Improved control and characterization of adjustable x-ray optics

Allured, Ryan, Ben-Ami, Sagi, Cotroneo, Vincenzo, Marquez, Vanessa, McMuldroch, Stuart, et al.

Ryan Allured, Sagi Ben-Ami, Vincenzo Cotroneo, Vanessa Marquez, Stuart McMuldroch, Paul B. Reid, Daniel A. Schwartz, Susan Trolier-McKinstry, Alexey A. Vikhlinin, Margeaux L. Wallace, "Improved control and characterization of adjustable x-ray optics," Proc. SPIE 9603, Optics for EUV, X-Ray, and Gamma-Ray Astronomy VII, 96031M (4 September 2015); doi: 10.1117/12.2186411

SPIE.

Event: SPIE Optical Engineering + Applications, 2015, San Diego, California, United States

Improved Control and Characterization of Adjustable X-ray Optics

Ryan Allured[a], Sagi Ben-Ami[a], Vincenzo Cotroneo[a], Vanessa Marquez[a], Stuart McMuldroch[a], Paul B. Reid[a], Daniel A. Schwartz[a], Susan Trolier-McKinstry[b], Alexey A. Vikhlinin[a], Margeaux L. Wallace[b]

[a]Harvard-Smithsonian Center for Astrophysics, Cambridge, MA, USA
[b]Pennsylvania State University, University Park, PA, USA

ABSTRACT

We report on improvements in our efforts to control and characterize piezoelectrically adjustable, thin glass optics. In the past, an optical profilometer and a Shack-Hartmann wavefront sensor have been used to measure influence functions for a flat adjustable mirror. An electronics system has since been developed to control > 100 actuator cells and has been used in a full calibration of a high-yield flat adjustable mirror. The calibrated influence functions have been used to induce a pre-determined figure change to the mirror, representing our first attempt at figure control of a full mirror. Furthermore, we have adapted our metrology systems for cylindrical optics, allowing characterization of Wolter-type mirrors. We plan to use this metrology to perform the first piezoelectric figure correction of a cylindrical mirror over the next year.

1. INTRODUCTION

The X-ray Surveyor is a mission concept that seeks to achieve sub-arcsecond angular resolution over a 10 arcminute field-of-view and roughly 30 times the effective area of the Chandra X-ray Telescope.[7] Such a mission would offer the ability to observe the early seeds of super massive black holes out to redshifts of $z \gtrsim 10$, allowing observers to discriminate between various theories of how these powerful objects formed.[15,16] Other exciting applications of an X-ray Surveyor include exploring the feedback mechanisms between evolution of SMBHs and their host galaxies, using high-resolution spectroscopy to probe plasma physics, and many others.

A crucial enabling technology for such a mission is the optics that produce the high angular resolution and effective area while minimizing mass and production costs. Thin shell, segmented optics represent a promising avenue towards the realization of such technology. Thin optics are able to be packed efficiently in a glancing incidence, Wolter telescope to maximize effective area while minimizing mass. The segmented approach enables cost-efficient production lines, greatly reducing the cost per optic. The primary technical challenges in producing thin shell optics are fabrication errors, mounting distortions, gravity release, and on-orbit thermal distortions. Various groups[4,10,13,14,18] have developed approaches to address these problems, but most cannot correct for all of them. In particular, there are few approaches that address the issues of mounting distortions, gravity release, and on-orbit thermal distortions.

Our approach is to make our mirrors piezoelectrically adjustable.[11] Our mirror substrates are made of Corning Eagle^{TM} glass and slumped to the nominal Wolter geometry (Wolter-Schwarzschild in the X-ray Surveyor case). A thin metallic coating, typically gold or iridium, is deposited on the concave surface to enable high X-ray reflectivity. On the convex surface, a series of coatings are used to enable electronic control of the mirror figure. A continuous platinum coating is first deposited in order to act as a ground electrode. A 1.5 μm lead zirconate-titanate (PZT) pieozelectric coating is deposited as the actuation mechanism.[17] Finally, pixelated platinum electrodes are deposited on top of the PZT in order for localized electric fields to be created over the surface of the mirror. When voltage is applied to one of the platinum cell electrodes, the resulting electric field induces an in-plane strain in the PZT layer, which results in a distortion over the mirror surface. This distortion becomes localized if the mirror is mounted in an over-constrained geometry. Additionally, work is on-going to develop ZnO thin-film transistors to enable row-column addressing of the actuator cells[9] and also on-cell strain gauges for localized strain and temperature feedback.[12] A schematic of the general approach is shown in Fig. 1, and a photograph of an early cylindrical prototype mirror is shown in Fig. 2.

Optics for EUV, X-Ray, and Gamma-Ray Astronomy VII, edited by Stephen L. O'Dell, Giovanni Pareschi,
Proc. of SPIE Vol. 9603, 96031M · © 2015 SPIE · CCC code: 0277-786X/15/$18 · doi: 10.1117/12.2186411

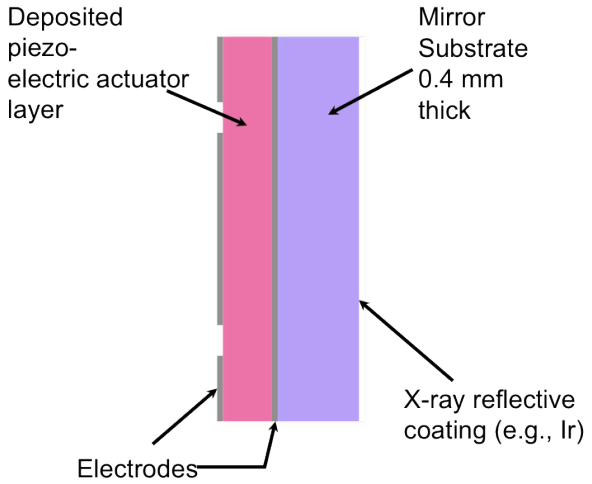

Figure 1. A conceptual diagram of the adjustable X-ray optics approach. The glass substrate is shown in purple with a non-visible X-ray reflective coating deposited on the optical surface. On the opposite surface, a $\sim$ 100 nm continuous Pt layer is deposited to act as a ground electrode. Then, a $\sim$ 1.5 µm lead zirconate-titanate piezoelectric layer is deposited. Finally, pixelated Pt electrodes are deposited to allow localized electric fields to be applied to the PZT coating. These fields induce strain in the PZT which allows control of the mirror figure.

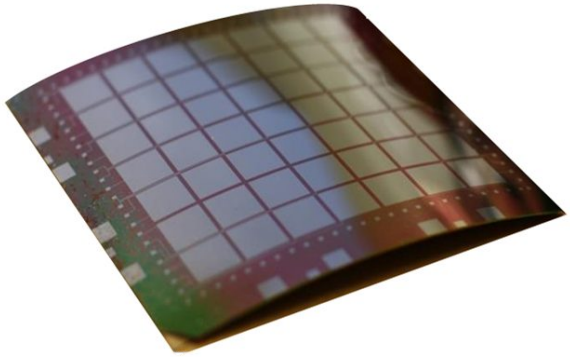

Figure 2. An early prototype of a cylindrical, piezoelectrically adjustable mirror. The radius of curvature is 220 mm, and the pre-slumped format of the glass substrate is 10 x 10 cm^2. The 7 x 7 array of 10 x 10 mm^2 Pt electrodes are connected via traces to pads at the mirror perimeter.

This paper reports on recent progress in the control and evaluation of prototype adjustable mirrors. A mathematical formalism based on Fourier analysis and simulation of mirror corrections is first reviewed to give context for the experimental work. The influence function calibration of a high-yield flat prototype sample and the results of introducing a pre-determined figure change to the sample are presented. Finally, the upgrade of the wavefront sensor metrology system for cylindrical optics is described along with plans for the first piezoelectric correction of a thin, cylindrical glass optic.

2. CORRECTION TRANSFER FUNCTION

The general mirror correction procedure requires both the measured figure error map of a mounted mirror and the influence functions, measured or theoretical, of all actuator cells to be used in the correction. An influence function is simply a two dimensional map of the distortions a given actuator cell introduces to a mirror for a given voltage, interpolated onto the same grid as the two dimensional figure error map. The amplitude of these maps is in the radial direction of the mirror. The sum of all influence functions, each weighted by an appropriate voltage, should ideally equal the inverse of the figure error map. This procedure is therefore a linear least squares problem, where the variable to be solved for is the vector of optimal correction voltages. Additional complications include a maximum constraint and a non-negative constraint for the influence functions. The maximum constraint is due to a maximum breakdown voltage of the actuator cells, and the non-negative constraint is due to the fact that the induced PZT strain is always tensile, regardless of the sign of the electric field.

Simulations of the correction of a flight-like mirror were previously reported as supporting evidence of the technique's feasibility.[1,2] Influence functions were computed using finite element analysis[6] for an X-ray Surveyor mirror segment with a 1 meter radius of curvature, 400 mm azimuthal span, and 200 mm axial length. Actuator cells were assumed to be 5 mm axially and 10 mm azimuthally with a 0.2 mm gap for a total of 1722 cells. These functions were computed over a 821 x 411 grid of points. Figure data was used from a mounted, hyperboloidal test mirror from the International X-ray Observatory program, interpolated onto the same grid as the influence

functions. The resulting figure error map is referred to as the "exemplar data." To estimate performance, the RMS axial slope was computed numerically from the figure data and then multiplied by $4\sqrt{2}$ to estimate the focal plane RMS diameter expected from two mirrors with equal but uncorrelated slope errors. The pre-correction performance was estimated to be 12.01 arcseconds. After optimizing actuator voltage amplitudes with a numerical least squares optimizer, the post-correction performance was estimated to be 0.4 arcseconds. Note that $< 25\%$ of the mirror perimeter area was excluded from the analysis; the influence functions have lower amplitudes and are less localized at the mirror edges, making this region difficult to correct and likely not usable for flight.

These simulations lent confidence that the PZT adjuster technique can correct a realistic mirror to sub-arcsecond performance. However, this was only a single realization of the infinite number of figure error maps that the adjusters may need to correct. In other words, it is not known prior to mounting and bonding what the final form of the mirror figure will be. Instead, the expected figure can be described using a power spectral density (PSD), the standard method of describing random surfaces in the optics community. The expected pre-correction mirror PSD can be predicted using a combination of metrology (for all spatial frequencies) and finite element analysis (for mounting and gravity distortion contributors at low spatial frequencies). It is therefore convenient to describe the ability to correct a mirror also in terms of spatial frequency.

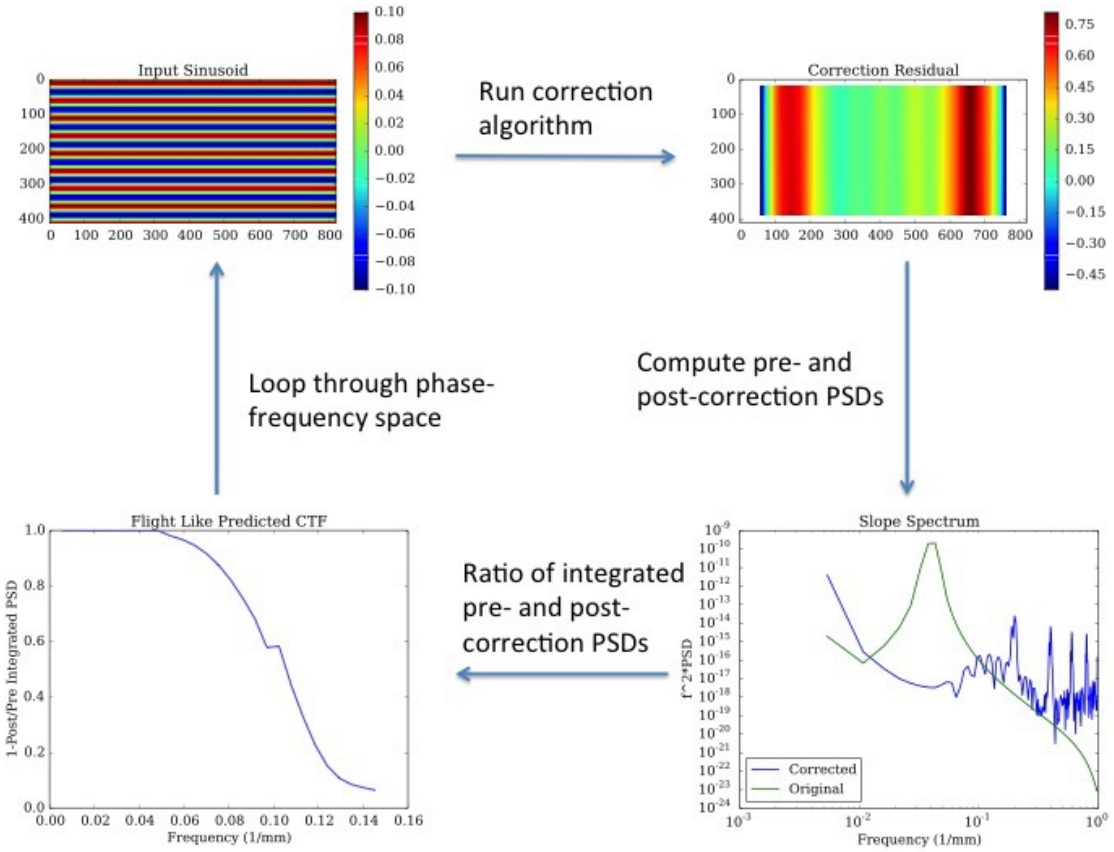

Figure 3. A flow chart of the correction transfer function calculation procedure.

A framework to arrive at a mathematical description of an adjustable mirror's ability to correct figure error is shown in Fig. 3. A theoretical figure error map is created on the same grid of points as the theoretical or measured influence functions for a given mirror geometry. This map is a simple axial sinusoid with a given amplitude, phase, and frequency. Azimuthal figure error has a reduced impact (typically by a factor of ~ 50) on the focal plane performance due to the glancing incidence geometry, therefore only axial figure error is considered. This

sinusoidal figure error map is used in the correction optimization algorithm along with the set of theoretical or measured influence functions to arrive at a corrected surface. The correction residuals are the difference between the achieved and desired corrections, and represent the residual surface error after correction. Then, the axial PSD is computed for both the input distortion map (pre-correction) and the residuals (post-correction). The ratio of the integrated post-correction PSD to the integrated pre-correction PSD is a measure of the ability to correct the input sinusoid. This is measured as a function of frequency by adjusting the frequency of the input sinusoid, and the result is a correction transfer function (CTF). This is defined as $1 - P_1/P_0$, where P_0 is the integrated PSD of the figure error map and P_1 is the integrated PSD of the correction residuals. The CTF for a flight-like simulated mirror is given in the lower left corner of Fig. 3.

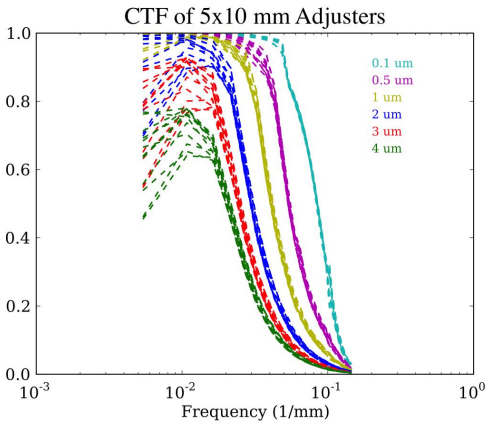

Figure 4. CTFs calculated for sinusoids of various amplitudes and phases. The color indicates the sinusoid amplitude. For each amplitude, the CTF was computed for different phases from 0 to 2π in 12 steps. Thus, 12 lines are present for each amplitude.

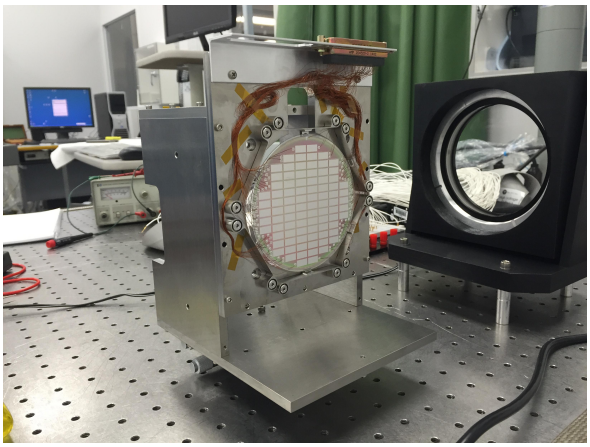

Figure 5. The DFC sample bonded into a six point flexure mount.

In the general linear least squares problem $Ax = b$, where x is the unknown vector to be solved for, if b is multiplied by a constant, then the solution x is multiplied by the same constant. Thus, a doubling of the input figure error in the correction algorithm will double the returned optimal voltages. This naturally introduces an amplitude dependence in the CTF based on the maximum and non-negative voltage constraints. As the amplitude of the input figure error of a given frequency increases, eventually the optimal voltages reach the maximum constraint and the ability to correct the figure decreases. This is clearly seen in Fig. 4, where CTFs for sinusoids of various amplitudes are plotted by color. Note that there is an amplitude below which the CTF ceases to be amplitude-dependent.

Furthermore, the CTF exhibits a phase dependence at low spatial frequencies primarily due to the tendency of influence functions to become less localized and exhibit lower amplitudes toward the mirror edges. If the mirror were of infinite axial extent and the influence functions well-described by a single kernel, this phase dependence would be nearly eliminated. The various lines for a given amplitude in Fig. 4 indicate different phases (from 0 to 2π), and the phase dependence is clearly indicated by the divergence of these lines at low spatial frequencies. The CTF shown in Fig. 3 is computed for a 0.1 μm amplitude and averaged over phase from 0 to 2π.

The exemplar data described above is representative of the expected figure error the adjustable optics technology must be able to correct. To determine whether the exemplar figure error is within the linear correction regime (i.e. amplitude-independent CTF), the correction algorithm was run using both the exemplar figure map and then the same map divided by two. If the figure error is in the linear correction regime, the residuals in the latter case should be exactly half of those of the former. The calculated residuals when using the halved exemplar figure error were 49.0% of those calculated using the original exemplar figure error. This result is evidence that the expected pre-correction figure error for adjustable mirrors is within the linear correction regime. In other words, the dynamic range of the actuator cells is large enough such that the required voltages to correct a flight-like mirror will likely lie within the maximum voltage constraints.

3. DETERMINISTIC FIGURE CONTROL MIRROR

Influence functions on both flat and cylindrical prototype mirrors have been previously measured using an optical profilometer[5] and most recently a wavefront sensor (WFS) metrology system.[2] Comparison of a WFS measurement of a central influence function on a flat mirror with the theoretical influence function computed with FEA produced an 8.7 nm RMS (38 nm peak-to-valley) agreement, which was within the metrology noise. The next step was to calibrate the full set of influence functions for a flat mirror and then use this data to introduce pre-determined figure changes to the full mirror surface.

A deterministic figure control (DFC) mirror was produced with a 1.5 μm PZT layer and 5 x 10 mm^2 platinum actuation electrodes. This mirror is considered high-yield, with only three of 88 actuators inoperable due to shorts to the ground electrode. This yield was achieved after a now-standard cell "resurrection" process[8] wherein 3 volts DC are applied to each cell in order to burn out short paths. The DFC substrate is a 0.4 mm thick, 100 mm diameter Corning Eagle^{TM} wafer. It is bonded to a six point flexure mount as shown in Fig. 5. Traces run from each actuator cell to pads at the perimeter of the mirror where Kapton-coated wires are bonded with conductive epoxy. The piezoelectric actuator cells were poled by the application of 5 volts DC for 15 minutes.

3.1 Influence Function Calibration

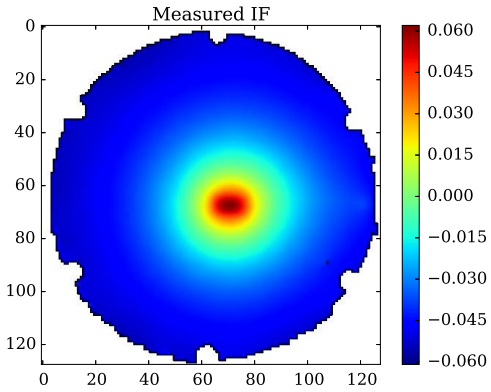

Figure 6. A measurement of a DFC central influence function. The color scale is in units of μm, where a positive value indicates a distortion along the outward normal of the reflective surface (i.e. the opposite surface to that which the PZT is deposited on). The roughly semi-circular regions at the mirror edges indicate the bonding points.

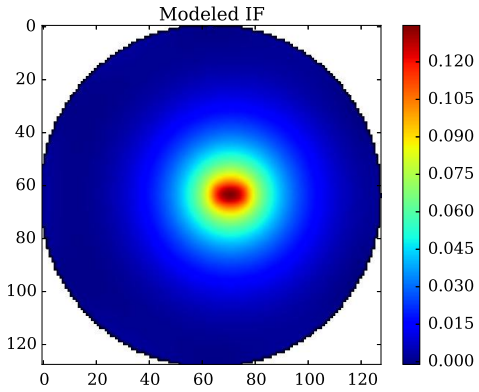

Figure 7. A finite element analysis model of the influence function from Fig. 6 with the same scale and sign convention.

In order to control all of the DFC actuator cells without the need to physically switch connections, an electronics system featuring the IRIS Smart Driver II - 128^{TM} was developed. The Smart Driver is a low noise, low power digital-to-analog controller with 128 channels. Since it is designed for operation up to 200 V, a LabJack U6 DAQ device was used to calibrate the low voltage output on each channel. The Smart Driver was connected to the DFC mirror through a plug-and-play protoboard. The Smart Driver is controlled through a Python-driven interface to a DLL.

The WFS metrology system is the same as previously used to measure and compare influence functions to FEA models. The system operates at 10 Hz and averaging is used to reduce metrology noise. A Python software development kit was used to automate influence function metrology with the Smart Driver voltage controller. For each influence function measurement, a reference measurement was taken as the average of 100 individual WFS measurements (10 second total acquisition) with no voltages applied to the mirror. Then, 5 volts were applied to a given cell and the influence function measurement acquired as the average of another 100 WFS measurements. The reference measurement was subtracted from the influence function measurement, and the

result saved to disk. This procedure was repeated for all 85 DFC influence functions. The measured influence function for a central cell is shown in Fig. 6, and the modeled influence function is shown in Fig. 7. The six bond points of the flexure mount can be seen in the measurement, along with a slight offset in the position of the cell. This offset is due to the platinum electrode mask being offset during deposition.

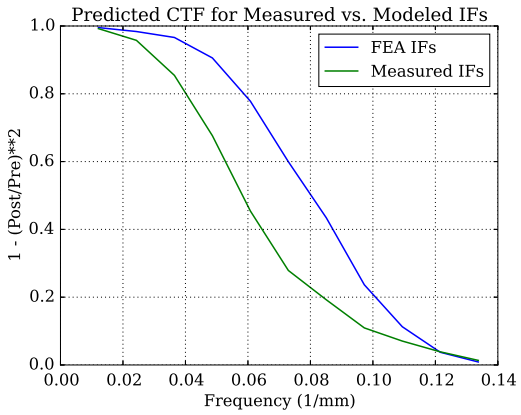

Figure 8. The predicted CTF for the DFC sample is presented using FEA modeled influence functions in blue and the measured influence functions in green. The measured influence functions have a degraded ability to introduce figure changes to the sample.

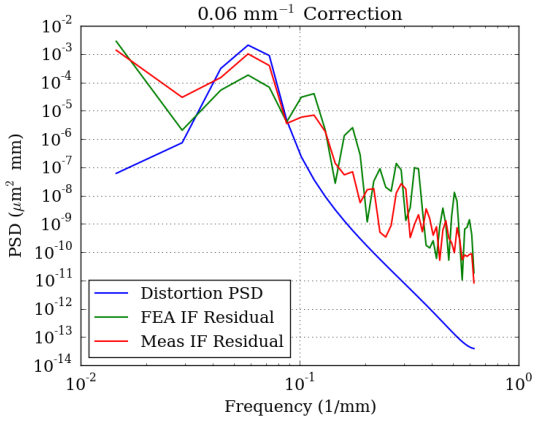

Figure 9. The PSDs of the input figure error (blue), the post-correction residual using FEA influence functions (green), and the post-correction residual using measured influence functions (red) are shown for the DFC sample. This example uses a 0.1 μm, 0.06 mm^{-1} sinusoid as the input figure error. There is a significant low frequency discrepancy between the residuals of the two correction methods. The high frequency content of the residuals is dominated by WFS metrology noise.

3.2 Predicted CTF

The procedure shown in Fig. 3 was repeated both with the calibrated and modeled DFC influence functions. The axial direction was taken to be the 5 mm actuator cell direction. A 0.1 μm amplitude sinusoid was used and the CTFs are averaged over phase from 0 to 2π. An analysis mask cutting out the perimeter of the mirror was used for the same reasons as with the flight-like CTF prediction. The resulting DFC CTFs are shown in Fig. 8, and there is a clear reduction in correction ability when using the measured influence functions. To shed light on the cause of this discrepancy, the correction at 0.06 mm^{-1} was investigated in more detail. The axial PSDs of the input sinusoid, the correction residuals using FEA influence functions, and the correction residuals using measured influence functions are all plotted in Fig. 9. The corrections should reduce the amplitude of the peak in the input sinusoid PSD. The correction using measured influence functions clearly has a stronger residual ripple at that frequency. At higher spatial frequencies, the difference between the two corrections is negligible and dominated by the high frequency WFS metrology noise. Thus, the reduced ability of the measured influence functions to induce figure changes to the mirror is due to low spatial frequency distortions. The theoretical figures achieved with the FEA correction and the measured correction methods are shown in Figs. 10 and 11, respectively. The low frequency distortions in the figure achieved with the measured influence functions are visually distinguishable from the relatively undistorted 0.06 mm^{-1} ripple in the FEA correction.

4. EXPERIMENTAL RIPPLE INTRODUCTION

Because the mounted figure of the DFC mirror is on the order of 100 μm peak-to-valley, the correction of the figure to sub-arcsecond axial slope was not possible. Thus, it is only possible to investigate relative figure changes due to piezoelectric adjustment. As a first attempt at controlling the full surface of a mirror with the piezoelectric adjusters, a pre-determined axial sinusoidal ripple of 0.3 μm amplitude and 0.02 mm^{-1} frequency was introduced to the DFC mirror.

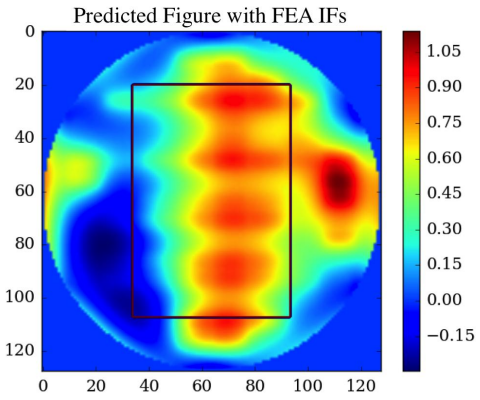

Figure 10. The residuals predicted by the correction algorithm for a 0.1 μm, 0.06 mm^{-1} sinusoid input figure using FEA modeled influence functions. The color scale is in μm.

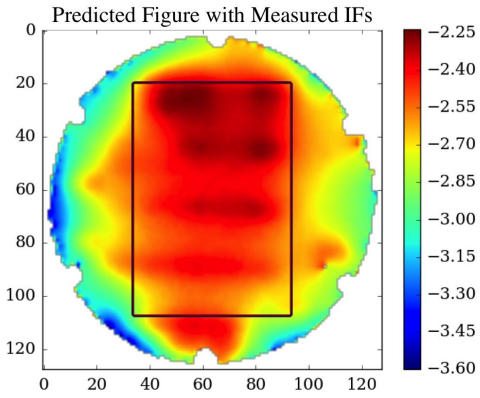

Figure 11. The residuals predicted by the correction algorithm for a 0.1 μm, 0.06 mm^{-1} sinusoid input figure using measured influence functions. The color scale is in μm.

The results of this experiment are shown in Fig. 12. Each plot represents the area of the DFC mirror within the analysis mask shown previously in Figs. 10 and 11. The axial slopes are shown (i.e. the axial derivative of the figure residuals). The color scale goes from +7.75 to -7.75 arcseconds for all four panels. The far left plot the input axial sinusoid. The axial RMS slope of this input sinusoid is 5.4 arcseconds. The remaining plots show correction residuals on the same color scale. The center-left plot shows the residuals between the input sinusoid and the predicted figure produced by the correction algorithm. This is what the algorithm predicts the adjusters can achieve, and the residuals have a 1.7 arcsecond RMS axial slope. The center-right plot shows the residuals between the input sinusoid and the measured figure after applying a correction to the DFC mirror in two iterations. The first iteration applied the voltages produced by the correction algorithm using the input sinusoid as the figure error map. The second iteration computed and applied perturbations to the correction voltages based on the measured residuals after the first iteration. The residuals between the input sinusoid and the measured figure after two correction iterations contain a 2.1 arcsecond RMS axial slope. Finally, the residuals between the second and third plots are presented in the far right plot, and represents the accuracy to which the predicted figure change was achieved. The experimental DFC ripple introduction achieved what the algorithm predicted to within a 0.9 arcsecond RMS axial slope.

The residuals in the far right plot in Fig. 12 are dominated by low spatial frequencies (the PSD is well-described by a power law with a slope of -2). Thus, as with the CTF predictions, low frequency distortions are degrading the ability of the DFC mirror to introduce figure changes. After the ripple introduction experiment described above, low frequency metrology distortions have been discovered due to the filtration blowers in the cleanroom where the experiment took place. By turning the blowers off, the standard deviation of the peak-to-valley influence function amplitude was reduced by a factor of ~ 4. The entire set up has been relocated to a dedicated clean tent wherein the blowers may be turned off for extended periods of time.

Hysteresis has also been discovered in the mirror actuation by observing the DFC mirror with a high sampling rate while turning cell voltages on and off. A residual influence function on the order of $\sim 10\%$ of the full amplitude remains after the voltage is reduced to zero and then decays to zero over the course of ~ 30 seconds. Despite the decay, it is possible the residual distortion after the measurement of an influence function could impact the measurement of the subsequent influence function. Hysteresis is a well-known phenomenon in piezoelectric materials, and this could potentially mean that the sample was not adequately poled prior to influence function calibration. A higher voltage and/or a higher poling temperature could reduce the level of hysteresis in this sample.

The various sources of low spatial frequency distortions in the DFC mirror calibration will be investigated in the near-term. The eventual goal is to reduce the low frequency distortions to a level where the experimental

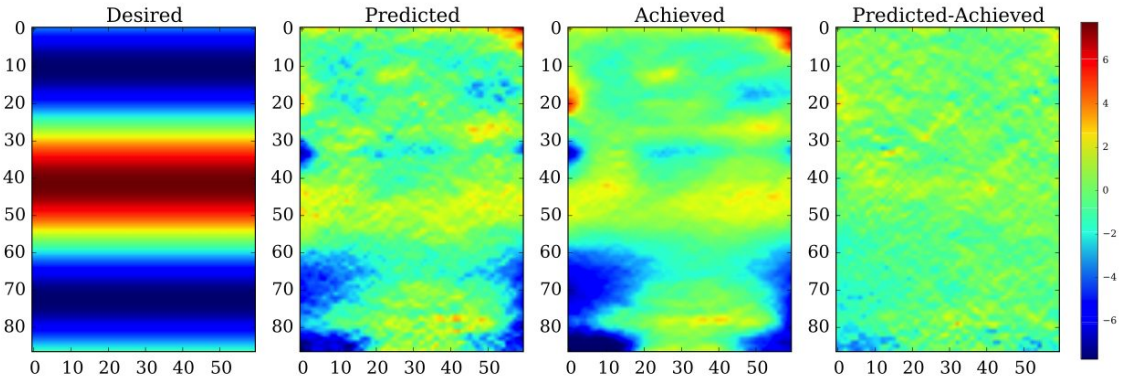

Figure 12. Axial slope residuals of the experimental ripple introduction. The color scale for all panels goes from +7.75 (red) to -7.75 arcseconds (blue). *Far left*: The goal sinusoid for the experimental ripple introduction. (5.4 arcsecond RMS slope) *Center left*: The residuals between the goal sinusoid and the figure predicted by the correction algorithm. (1.7 arcsecond RMS slope) *Center right*: The residuals between the goal sinusoid and the measured figure after a two-iteration correction. (2.1 arcsecond RMS slope) *Far right*: The residuals between the predicted post-correction figure and the measured post-correction figure. (0.9 arcsecond RMS slope)

CTF approaches that using the theoretical FEA influence functions, and also to reduce the ripple introduction residuals to within the WFS metrology noise. This will serve as a validation of our general adjustable optics modeling techniques.

5. CYLINDRICAL METROLOGY SYSTEM

The work with flat adjustable optics prototypes in conjunction with flight-like mirror modeling has provided confidence that this technique is a feasible approach toward lightweight, sub-arcsecond X-ray optics. The overall goal of the project, however, is to fabricate and correct Wolter-type optics to a sub-arcsecond telescope performance. Our next milestone is the fabrication and correction of a cylindrical mirror to an equivalent sub-arcsecond RMS diameter telescope performance, requiring a mirror axial RMS slope < 0.2 arcseconds. Achieving this milestone will require a cylindrical slumped glass mirror with adequate starting figure to allow the piezoelectric adjusters to correct the mirror to this level.

In addition to an adequate mirror substrate, PZT actuator deposition, and deposition of a low-stress reflective coating,[3] this work requires a metrology system capable of measuring a 1 meter radius of curvature cylinder. The WFS metrology system used in the flat mirror influence function calibrations has been adapted for cylindrical optics. The mirrors being slumped at the Smithsonian Astrophysical Observatory have a 220 mm radius of curvature, so the adaptation features a computer generated hologram (CGH) that transforms an incident plane wave into a converging 200 mm radius of curvature cylindrical wave. The optical design is shown in Fig. 13, where the cylindrical axis is vertical in the top view and is orthogonal to the plane of the page in the bottom view. The cylindrical CGH acts as a cylindrical null lens, and is positioned after the spherical collimation lens. The resulting cylindrical wave converges to a line focus and then diverges to illuminate a concave 220 mm radius of curvature at normal incidence. The wave is retroreflected and passes back through the cylindrical CGH, the collimator lens, the spherical field lens, the cylindrical field lens, and finally enters the WFS. The cylindrical CGH breaks the symmetry in the tangential and sagittal axes, and therefore the cylindrical field lens is necessary to ensure the curved mirror is imaged at the same axial location in either axis. A weak cylindrical lens with a 1 meter focal length is used in this design. For the experiment described above, a new CGH is needed to create a

slower cylindrical beam, and the cylindrical field lens will require a modified axial position and/or focal length to maintain adequate imaging of the test optic in both axes.

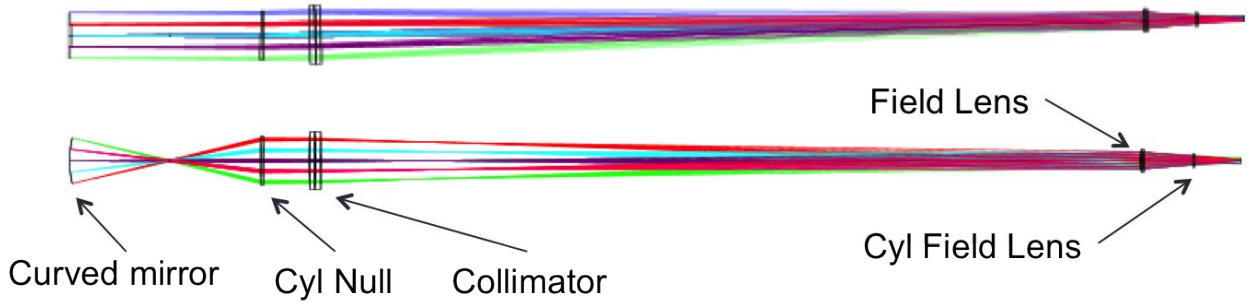

Figure 13. The ZEMAX optical design of the cylindrical WFS system. The cylindrical axis is orthogonal to the plane of the page in the bottom view, where the effect of the cylindrical CGH is clearly seen. In the top view, the system is rotated 90 degrees to show the optical axis in which the cylindrical optics have no effect.

6. SUMMARY AND FUTURE PLANS

We have developed a quantitative measure of a piezoelectrically adjustable mirror's ability to correct figure error as a function of spatial frequency—the correction transfer function. This framework has been used to evaluate the performance of a high-yield, flat adjustable mirror prototype. Low spatial frequency distortions in the influence function measurements degrade the ability of this mirror to correct figure error, particularly at higher frequencies. Potential sources of error have been identified, and the low frequency distortions will be investigated and reduced in the near future. We have adapted our wavefront sensor metrology system for the measurement of cylindrical optics, and we plan to use this system to correct a cylindrical piezoelectrically adjustable mirror over the course of the next year.

ACKNOWLEDGMENTS

This work was supported by NASA Grant NNX13AD46G and also by internal funding from the Smithsonian Astrophysical Observatory, a division of the Smithsonian Institution.

REFERENCES

[1] Aldcroft, T. L., Schwartz, D. A., Reid, P. B., Cotroneo, V., & Davis, W. N. 2012, Proc. SPIE, 8503, 85030F
[2] Allured, R., Cotroneo, V., Johnson-Wilke, R., et al. 2014, Proc. SPIE, 9144, 91441D
[3] Ames, K., Bruni, R., Reid, P. B., & Romaine, S. E. 2015, Proc. SPIE 9603
[4] Chalifoux, B., Heilmann, R. K., & Schattenburg, M. L. 2014, Proc. SPIE, 9144, 91444D
[5] Cotroneo, V., Davis, W. N., Marquez, V., et al. 2012, Proc. SPIE, 8503, 850309
[6] Davis, W. N., Reid, P. B., & Schwartz, D. A. 2010, Proc. SPIE, 7803, 78030P
[7] Gaskin, J. A. et al. 2015, Proc. SPIE, 9601
[8] Johnson-Wilke, R. L., Wilke, R. H. T., Cotroneo, V., et al. 2012, Proc. SPIE, 8503, 85030A
[9] Johnson-Wilke, R. L., Wilke, R. H. T., Wallace, M., et al. 2014, Proc. SPIE, 9208, 920809
[10] Ramsey, B. D., Atkins, C., Gubarev, M. V., Kilaru, K., & O'Dell, S. L. 2013, Nuclear Instruments and Methods in Physics Research A, 710, 143
[11] Reid, P. B., Aldcroft, T. L., Allured, R., et al. 2014, Proc. SPIE, 9208, 920807
[12] Reid, P. B. et al. 2015, Proc. SPIE, 9603
[13] Sung, E., Chalifoux, B., Schattenburg, M. L., & Heilmann, R. K. 2013, Proc. SPIE, 8861, 88610R

[14] Ulmer, M. P., Wang, X., Knapp, P., et al. 2014, Proc. SPIE, 9208, 920808
[15] Vikhlinin, A., Reid, P., Tananbaum, H., et al. 2012, Proc. SPIE, 8443, 844316
[16] Vikhlinin, A. 2014, AAS/High Energy Astrophysics Division, 14, #401.01
[17] Wilke, R. H. T., Johnson-Wilke, R. L., Cotroneo, V., et al. 2013, App. Opt. 52, 3412
[18] Zhang, W. W., Biskach, M. P., Bly, V. T., et al. 2014, Proc. SPIE, 9144, 914415